Lattice dynamics and magnetic exchange interactions in GeCo$_2$O$_4$: A spinel with $S = \frac{1}{2}$ pyrochlore lattice

Prativa Pramanik [1,*] Sobhit Singh [2,*,†] Mouli Roy Chowdhury,[1] Sayandeep Ghosh [1] Vasant Sathe,[3]
Karin M. Rabe,[2] David Vanderbilt [2] Mohindar S. Seehra [4] and Subhash Thota [1,‡]

[1]*Department of Physics, Indian Institute of Technology Guwahati, Assam 781039, India*
[2]*Department of Physics and Astronomy, Rutgers University, Piscataway, New Jersey 08854-8019, USA*
[3]*UGC DAE Consortium for Scientific Research, Indore- 452 001, India*
[4]*Department of Physics and Astronomy, West Virginia University, Morgantown, West Virginia 26506, USA*

GeCo$_2$O$_4$ is a unique system in the family of cobalt spinels ACo$_2$O$_4$ (A= Sn, Ti, Ru, Mn, Al, Zn, Fe, etc.) in which magnetic Co ions stabilize on the pyrochlore lattice exhibiting a large degree of orbital frustration. Due to the complexity of the low-temperature antiferromagnetic (AFM) ordering and long-range magnetic exchange interactions, the lattice dynamics and magnetic structure of a GeCo$_2$O$_4$ spinel have remained puzzling. To address this issue, here we present theoretical and experimental investigations of the highly frustrated magnetic structure, and the infrared (IR) and Raman-active phonon modes in the spinel GeCo$_2$O$_4$, which exhibits an AFM ordering below the Néel temperature $T_N \sim 21$ K and an associated cubic ($Fd\bar{3}m$) to tetragonal ($I4_1/amd$) structural phase transition whose location at T_N vs at a lower $T_S \sim 16$ K is controversial. Our density functional theory (DFT+U) calculations reveal that one needs to consider magnetic-exchange interactions up to the third-nearest neighbors to get an accurate description of the low-temperature AFM order in GeCo$_2$O$_4$. At room temperature, three distinct IR-active modes (T_{1u}) are observed at frequencies 680, 413, and 325 cm^{-1} along with four Raman-active modes A_{1g}, $T_{2g}(1)$, $T_{2g}(2)$, and E_g at frequencies 760, 647, 550, and 308 cm^{-1}, respectively, which match reasonably well with our DFT+U calculated values. All the IR-active and Raman-active phonon modes exhibit signatures of moderate spin-phonon coupling. The temperature dependence of various parameters, such as the shift, width, and intensity, of the Raman-active modes is also discussed. Noticeable changes around $T_N \sim 21$ K and $T_S \sim 16$ K are observed in the Raman line parameters of the E_g and $T_{2g}(1)$ modes, which are associated with the modulation of the Co-O bonds in CoO$_6$ octahedra during the excitations of these modes.

I. INTRODUCTION

The diversity in the properties and applications of spinels with the general formula of AB$_2$O$_4$ arises from the variety of cations, magnetic or nonmagnetic, that can be substituted at the tetrahedral A-sites and octahedral B-sites of the spinel structure [1–9]. Recent studies on a subclass of spinels having nonmagnetic cations such as Zn^{2+}, Mg^{2+}, and Ge^{4+} at the A-sites and magnetic cations at the B-sites reveal intriguing magnetic and structural properties at low temperatures. As first pointed out by Anderson [10], these spinels have inherent magnetic frustration, making the long-range magnetic order, if at all present, highly dependent on various other factors [4–6,9,11]. Examples of such spinels are ZnFe$_2$O$_4$ [12], defect spinel MgMnO$_3$ [13], and GeCo$_2$O$_4$ [14,15]. The latter is the subject of this paper. It is noteworthy that GeCo$_2$O$_4$, hereafter listed as GCO for brevity, has been substantially investigated in connection with its use as an anode material for Li-ion batteries [16–19]. Moreover, the nanostructures of

GCO have found applications in the renewable energy sectors such as fuel cells, electrochemical sensors, and supercapacitors [17,19].

The magnetic properties of GCO have been under intense investigation in recent years because of the distinct magnetoelectric features linked to the noncollinear spin arrangement and distorted cubic structure. Based in part on several previous electron-spin resonance, magnetic, and neutron diffraction studies in GCO [14,20–28], Pramanik *et al.* [15] recently presented results on the magnetic ground state, magnetic-field-induced transitions, and optical band gap of GCO. Summarizing these results, it was shown that GCO contains a pyrochlore lattice of Co^{2+} spin moments which have effective spin $S = 1/2$ (instead of $S = 3/2$ as expected from the Hund's rules) due to the effects of the spin-orbit coupling and Jahn-Teller distortion. The magnetic ordering consists of alternate planes of kagome (KGM) and triangular (TRI) spins lying perpendicular to the [111] direction. The dominant in-plane exchange constant between the Co^{2+} spins is ferromagnetic (FM). However, the spins in the neighboring planes are ordered antiferromagnetically (AFM) with **q** $= (\frac{1}{2}, \frac{1}{2}, \frac{1}{2})$ to yield an overall AFM order in the absence of any external magnetic field below the Néel temperature $T_N = 20.4$ K [15]. Due to such a peculiar magnetic behavior,

*These authors contributed equally to this work.
†Corresponding author: sobhit.singh@rutgers.edu
‡Corresponding author: subhasht@iitg.ac.in

especially owing to the frustrated AFM ordering with $\mathbf{q} = (\frac{1}{2}, \frac{1}{2}, \frac{1}{2})$, various exotic competing magnetic phases such as classical and quantum spin liquid phases, recently reported in (111)-oriented quasi-two-dimensional spinels through a geometric lattice design approach, can be realized in GCO at low temperatures [11,29,30].

Several studies reported a cubic ($Fd\bar{3}m$) to tetragonal ($I4_1/amd$) distortion of the lattice accompanying T_N [25,31,32], although high-resolution x-ray diffraction studies by Barton *et al.* [26] revealed that the tetragonal distortion of $\sim$0.1% in the lattice parameters occurs at $T_S = 16$ K, a few degrees below T_N, along with modulation of the Co-O bonds in the CoO$_6$ octahedra. However, it likely has a nonmagnetic origin since no anomalies occur in the heat capacity and magnetic susceptibility data near T_S [26]. Also, the degree of tetragonality progressively increases with decreasing temperature [26]. This cubic-to-tetragonal structural phase transition was attributed to local Jahn-Teller effects [26], which lift the degeneracy of the t_{2g} states by minimizing the energy of the d_{xz} and d_{yz} Co-3d suborbitals [33]. The closeness between the magnetic and structural transition temperatures reveals the existence of competing spin-orbit coupling and Jahn-Teller effects in GCO [26,31–33]. Currently, there exists a fair amount of debate regarding the fact that T_S is below the T_N, which is uncommon when compared to other spinels that exhibit magnetostructural quantum phase transitions [34–46].

A systematic investigation of the temperature-dependent lattice dynamics is required to pin down the nature of transitions occurring near T_S and T_N in GCO. The only previously reported Raman studies in GCO are those of Koringstein *et al.* [47], which reported the observation of three Raman-active modes [A_{1g}, $T_{2g}(1)$, and E_g] in GCO. However, these studies were done at only two temperatures, 200 and 400 K, which are much higher than the T_S and T_N. Also, the only yet reported infrared (IR) study in GCO was performed by Preudhomme and Tarte [48] at 300 K, which reported the observation of four IR-active modes (T_{1u}).

In this work, we perform detailed temperature-dependent Raman measurements covering the temperature range of 5 to 300 K with a focus on the changes occurring in the Raman-active modes as the temperature is lowered through T_N and T_S. Notably, our low-temperature Raman measurements confirm that the structural phase transition in GCO follows the magnetic phase transition, as first reported by Barton *et al.* [26] using x-ray diffraction measurements. We observe noticeable changes in the line parameters of the E_g and T_{2g} modes, which are associated with the modulation of the Co-O bonds in CoO$_6$ octahedra, near the T_N and T_S. We further report the observation of three (out of four) symmetry-allowed IR-active T_{1u} modes along with two satellite modes likely appearing due to the local symmetry breaking. In addition, computational studies of the lattice modes using density functional theory (DFT+U) calculations are presented, revealing the presence of moderate spin-phonon coupling in GCO. A systematic analysis of the Heisenberg spin Hamiltonian suggests that the magnetic-exchange interactions up to the third-nearest neighbors are required to accurately describe the low-temperature AFM ordering in GCO. In addition, we also briefly comment on the problems encountered in the DFT+U calculations

involving the orbital occupation of Co-3d orbitals located at the magnetically frustrated sites in GCO.

This paper is organized as follows. In Sec. II, experimental and computational details of this study are presented. Section III contains all the results and discussions in the following order: first we discuss the crystal structure and the magnetic-exchange interactions in GCO, and then we present our theoretical and experimental investigations on the lattice dynamics of GCO. This is followed by conclusions in Sec. IV.

II. METHODS

A. Experimental details

A well-ground mixed powder of high-purity GeO$_2$ (Sigma-Aldrich, 99.99%) and Co$_3$O$_4$ (Sigma-Aldrich, 99.99%) in stoichiometric amounts was pressed into a cylindrical disk at 50 kg/cm^2 using a hydraulic press and followed by the sintering process to yield the desired compound. The details of the sample synthesis procedures are described in a previous publication [15]. The single phase of the synthesized sample was confirmed by x-ray diffraction measurements using a high-resolution XPERT-PRO diffractometer (Co-K$_\alpha$ radiation with $\lambda = 1.78901$ Å). The temperature-dependent vibrational Raman-scattering spectra of GCO were recorded with a commercial Labram-HR800 micro-Raman spectrometer, in the temperature range of 5 to 300 K, using a He-Ne laser of wavelength 514 nm. For frequency calibration, the silicon mode at 520 cm^{-1} was used. All the Raman spectra were recorded in the anti-Stokes region. For the low-temperature measurements, the sample was first mounted on a cold stage setup (THMS600 stage, Linkam, UK) equipped with a temperature controller capable of maintaining a steady temperature. The sample was cooled by liquid helium and the temperature controller was able to hold the temperature fluctuations within a range of $\pm$1 K. The experimental uncertainty in the Raman peak positions, as determined using Lorentzian oscillator fits, was less than 0.1 cm^{-1}. The room-temperature IR spectrum was recorded using a Perkin-Elmer Spectrum-Two system with the standard spectral resolution of 0.5 cm^{-1}. The IR-active mode frequencies were determined by Lorentzian oscillator fits of the transmittance data.

B. Computational details

In order to better understand the nature of the magnetic-exchange interactions and Raman and IR-active phonon modes in GCO, we carried out DFT+U-based first-principles calculations using the projector augmented wave (PAW) method as implemented in the VASP software [49–51]. The PAW pseudopotentials considered the following valence configurations: Ge 4$s^2$4p^2, Co 3$d^8$4s^1, and O 2$s^2$2p^4. A kinetic energy cutoff of 650 eV was set for the plane waves. The reciprocal space was sampled using a Monkhorst-pack k mesh [52] of size 8 × 8 × 8. The energy convergence criterion for the self-consistent DFT+U calculations was set to 10^{-7} eV, and the force convergence criterion for relaxation calculations was set to 10^{-3} eV/Å. All DFT+U calculations were performed for collinear magnetic configurations without considering spin-orbit coupling effects. The PYPROCAR software [53] was used to plot the density of states, shown in the

Supplemental Material (SM) [54]. We used the PHONOPY package to study the lattice dynamics [55]. Supercells of size $2 \times 2 \times 2$ were employed to calculate the phonon frequencies and phonon eigenvectors within the finite-displacement approach. The exchange-correlation functional was computed using the generalized-gradient approximation (GGA) as parameterized by Perdew-Burke-Ernzerhof (PBE) as well as the PBE revised for solids (PBEsol) [56,57]. We find that the PBEsol yields lattice parameters and phonon frequencies that are in better agreement with the experimental data as compared to the PBE predictions.

The on-site Coulomb interaction effects for Co-3d electrons were treated at the mean-field level using the rotationally invariant DFT+U method introduced by Liechtenstein *et al.* [58]. We set $U = 4.0$ eV and $J = 1.0$ eV [14]. We find that this set of values appropriately describes the lattice parameters, magnetic structures, and vibrational properties of GCO. No tuning of the (U, J) parameters was performed to match the calculated phonon frequencies with the experimental data. In addition, it has been reported that an effective $U_{\text{eff}}^{\text{Co}}(= U - J)$ in the range of 2–3 eV provides a reasonable prediction of the electronic structure and optical properties of GCO [14].

We often noticed an anomalous variation in the occupation of the Co-3d orbitals in some of our DFT+U calculations due to the presence of strong magnetic frustration effects leading to a metastability problem in this system [59,60]. To ensure the correct and consistent occupation of the Co-3d orbitals, we utilized the occupation matrix control methodology developed by Allen and Watson [60] in our reported DFT+U calculations. We optimized the structural primitive cell in the FM order since the FM order preserves the cubic symmetry of the paramagnetic phase. The PBE+U and PBEsol+U optimized lattice parameters are 8.434 and 8.322 Å, respectively. We observed that the PBEsol+U optimized lattice parameters are in excellent agreement with the reported experimental data (8.3191 Å) [15,26]. Further, the PBEsol+U optimized Co-O and Ge-O bond lengths are 2.1 Å and 1.8 Å, respectively, which agree very well with the reported experimental data (2.1 Å and 1.8 Å) [15,21,26].

III. RESULTS AND DISCUSSION

A. Crystal structure and magnetic structure of GeCo$_2$O$_4$

GeCo$_2$O$_4$ [(Ge^{4+})$_A$[Co$_2^{2+}$]$_B$O$_4$] crystallizes in a normal cubic spinel structure at room temperature (space group $Fd\bar{3}m$). The oxygen anions are located at the 32e Wyckoff positions forming a close-packed face-centered-cubic arrangement, whereas Ge and Co cations occupy the 8a-tetrahedral and 16d-octahedral interstitial positions, respectively. Therefore, the crystal structure consists of the corner-sharing CoO$_6$ octahedra and GeO$_4$ tetrahedra, as shown in Fig. 1(a). The structural primitive cell contains two formula units of GCO. There are four magnetic Co atoms in the primitive cell forming a regular Co-Co tetrahedron, where each Co is located at the center of an oxygen octahedron at the 16d sites. The corner-sharing oxygen octahedra form a pyrochlore lattice containing alternating planes of the KGM and TRI layers of
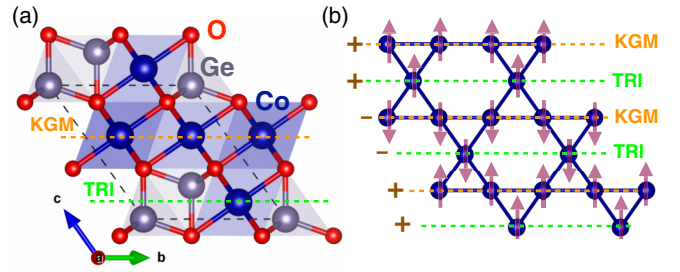

FIG. 1. (a) Crystal structure of GCO. Dashed black lines mark the boundaries of the structural primitive cell. The primitive cell consists of two GeO$_4$ tetrahedra and one Co$_4$ tetrahedral unit. Here Co, Ge, and O ions are presented by the blue, gray, and red color, respectively. (b) Schematic representation of $\mathbf{q} = (\frac{1}{2}, \frac{1}{2}, \frac{1}{2})$ AFM ordering in GCO. Magnetic moments at the Co sublattice are shown using arrows in a collinear setting, i.e., majority or up (+) and minority or down (−) spin states are denoted using up and down arrows, respectively. Alternating kagome (KGM) and triangular (TRI) planes are highlighted using dashed horizontal lines. A $T_+ K_+ T_- K_- T_+ K_+ T_- K_- \cdots$-type AFM spin configuration of TRI ($T_\pm$) and KGM ($K_\pm$) layers can be noticed along the [111] direction.

Co atoms stacked along the [111] direction of the bulk unit cell.

There are three Co atoms in the KGM plane and one Co atom in the TRI plane, as shown in Fig. 1(a). Within each of the KGM and TRI planes, Co spins order ferromagnetically. However, the overall low-temperature magnetic structure of GCO is very complex, involving an antiferromagnetic ordering of wave vector $\mathbf{q} = (\frac{1}{2}, \frac{1}{2}, \frac{1}{2})$. In this AFM order, Co spins in a pair of TRI and KGM layers (i.e., within a structural primitive cell) order ferromagnetically, whereas the same order antiferromagnetically in the neighboring structural primitive cell, thus resulting in a TRI-KGM layer spin configuration of $T_+ K_+ T_- K_- T_+ K_+ T_- K_- \cdots$ along the [111] direction, as shown in Fig. 1(b). Here, T_+ (T_-) and K_+ (K_-) denote the spin-up (-down) configurations of the TRI and KGM layers, respectively.

To get an accurate description of the low-temperature magnetic structure experimentally reported in Ref. [15], we extract the values of the spin-exchange interactions (J's) by mapping the DFT-computed total energies onto a Heisenberg spin Hamiltonian [Eq. (1)]. In our spin model, we consider four exchange-interaction parameters, which correspond to the first- (J_1), second- (J_2), and third- (J_3 and J_3') nearest-neighbor (NN) interactions, as shown in Fig. 2(a). The first-, second-, and third-NN interactions correspond to a Co-Co bond distance of 2.94, 5.09, and 5.86 Å, respectively. The third-NN interaction was further divided into two categories: J_3 and J_3'. Although both belong to the same Co-Co distance, J_3 connects two Co atoms located at 5.86 Å distance apart without passing through any intermediate Co atom, whereas J_3' connects two Co atoms located at 5.86 Å distance apart but it passes through an intermediate Co atom at the half bond distance. For instance, a J_3' exchange would correspond to the interaction between two Co atoms located at two adjacent TRI planes, with the bond between them passing through an intermediate Co atom situated at a KGM plane [see Fig. 2(a)].
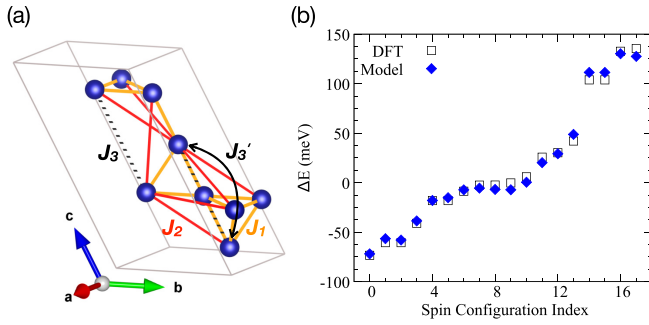
FIG. 2. (a) Definition of all four magnetic-exchange interactions, i.e., first- (J_1), second- (J_2), and third- (J_3 and J_3') NN, considered in this work. Co atoms are shown in blue color. Ge and O atoms are omitted for clarity. Note that J_3' passes through an intermediate Co atom (see text). (b) Fitting of the DFT (PBEsol+U) energy values computed for various different spin configurations in a doubled primitive cell, as shown in (a), with our model spin Hamiltonian. Here, we decide to choose the PBEsol+U method since it predicts better lattice parameters compared to the PBE+U predictions.

The spin Hamiltonian reads

$$H = E_0 + J_1 \sum_{<ij>}^{\text{first NN}} S_i \cdot S_j + J_2 \sum_{<ij>}^{\text{second NN}} S_i \cdot S_j$$
$$+ J_3 \sum_{<ij>}^{\text{third NN}} S_i \cdot S_j + J_3' \sum_{<ij>}^{\text{third NN}} S_i \cdot S_j, \quad (1)$$

where S_i and S_j denote the spin ordering at different Co sites, and E_0 represents a rigid shift in the total energy (E). In Fig. 2(b), we show the fitting of the DFT+U energies ($\Delta E = E - E_0$) computed for several distinct spin configurations in a doubled primitive cell, as shown in Fig. 2(a), with our spin Hamiltonian described in Eq. (1). The lowest-energy spin configuration corresponds to a $T_+ K_+ T_- K_- T_+ K_+ T_- K_- \cdots$-type AFM order, as shown in Fig. 1(b). This spin configuration represents a $\mathbf{q} = (\frac{1}{2}, \frac{1}{2}, \frac{1}{2})$ AFM order that has been experimentally observed in GCO [15]. We note that all the considered spin configurations yielded gapped densities of states, shown in SM [54], in their converged electronic ground state. This ensured that our DFT+U calculations correctly converged for all of the distinct spin configurations considered in this study.

The best fit of the data (provided in the SM [54]) yields $J_1 S^2 = -3.9$, $J_2 S^2 = 0.7$, $J_3 S^2 = 2.0$, and $J_3' S^2 = 0.4$ (in meV units), where positive (negative) values represent AFM (FM) magnetic interactions. We notice that the first-NN exchange has a dominating FM nature, whereas all the second- and third-NN interactions exhibit an AFM nature, which is consistent with the recent experimental observations [15]. According to the Goodenough-Anderson-Kanamory rules [1,10,61–65], J_1 is mediated via an intermediate oxygen ion having a Co-O-Co bond angle of $\theta = 90°$. Therefore, it is a superexchange interaction of FM nature. All other higher-order exchange interactions, viz., J_2, J_3, and J_3', are super-super AFM exchange interactions as they involve more than one ion along the exchange path. These competing FM and AFM exchange interactions are primarily responsible for introducing

the magnetic frustration and establishing a $\mathbf{q} = (\frac{1}{2}, \frac{1}{2}, \frac{1}{2})$ AFM order in GCO at low temperatures [22].

Our theoretical findings discussed above, when combined with the experimental results reported in Ref. [15], provide a firm foundation for the magnetic properties of GCO. Hereafter, we focus on the lattice dynamics and vibrational properties of GCO.

B. Lattice dynamics and vibrational spectroscopy in GeCo$_2$O$_4$

The vibrational spectroscopy of AB$_2$O$_4$ cubic spinels was first studied by Waldron, who analyzed the phonon modes of simple ferrites (AFe$_2$O$_4$) using the structural primitive cell having 14 atom per cell [66]. Later, White and DeAnglis presented a group theoretical approach to analyze the Raman spectra of cubic spinels by considering the rhombohedral lattice as the smallest Bravais cell [67]. In their study, they considered the body diagonal elements consisting of two AO$_4$ and one B$_4$ tetrahedron of 14 atoms total [67], as shown in Fig. 1(a). According to theory, the $Fd\bar{3}m$ space group belongs to the O_h^7 spectroscopic symmetry, whereas Ge^{4+}, Co^{2+}, and O^{2-} ions belong to the T_d, D_{3d}, and C_{3v}(32 e-sites) point groups, respectively [67]. All the allowed optical phonon modes at the Brillouin-zone center Γ ($\vec{k} = 0$) for each atomic displacement in the structural primitive cell can be denoted as [67,68]

$$\Gamma_{\text{vib}} = A_{1g} \oplus 2A_{2u} \oplus E_g \oplus 2E_u \oplus T_{1g}$$
$$\oplus 4T_{1u} \oplus 3T_{2g} \oplus 2T_{2u}. \quad (2)$$

Out of the 39 optical phonon modes, only five modes are Raman active ($A_{1g} \oplus E_g \oplus 3T_{2g}$), four modes ($4T_{1u}$) are IR active, and the remaining modes are inactive in simple Raman and IR experiments. We note that the acoustic modes transform according to the T_{1u} irreducible representation of the O_h point group. The atomic vibration patterns corresponding to the IR-active modes are shown in Fig. 3 and those of the Raman-active modes are shown in Fig. 4. These vibrational patterns, i.e., the phonon eigenvectors at Γ depicted using green arrows, were obtained using the PHONOPY package [55]. In addition, we note that in the case of the cubic-to-tetragonal phase transition, splitting of some phonon degeneracies occurs due to the reduction in the crystal symmetry. For instance, a triply degenerate T_{1u} phonon mode splits into a doublet (E_u) and a singlet (A_{2u}) during the cubic-to-tetragonal phase transition in GCO. However, the total number of phonon modes remains the same since the cubic-to-tetragonal phase transition is primarily driven by a zone-center Γ_3^+ mode.

As mentioned earlier, the magnetic structure of GCO is quite complex due to the $\mathbf{q} = (\frac{1}{2}, \frac{1}{2}, \frac{1}{2})$ AFM ordering, and a first-principles DFT+U calculation of the full phonon dispersion for the actual magnetic cell would be computationally very demanding. However, the DFT+U calculation for the structural primitive cell (14 atoms/cell) considering various different spin configurations can provide useful insights about the Raman/IR-active phonon modes at the zone-center Γ (which is required for this study), and the strength of the spin-phonon coupling in GCO.

To simulate the high-temperature paramagnetic phonon frequencies (at the infinite-temperature limit of spin

TABLE I. List of IR-active modes and their frequencies (in cm^{-1}) at room temperature for several cubic spinels.

	$T_{1u}(1)$	$T_{1u}(2)$	$T_{1u}(3)$	$T_{1u}(4)$	Reference
$GeCo_2O_4$	680	413	325		This work (Experiment)
$GeCo_2O_4$	# 640	407	312	189	This work (Calculation)
	* (615)	(379)	(294)	(168)	# PBEsol+U; * (PBE+U)
$GeCo_2O_4$	679	427	321	186	[48]
$GeNi_2O_4$	690	453	335	199	[48]
$GeMg_2O_4$	694	450	485	274	[48]
$SiCo_2O_4$	815	504	354	161	[74]
$SiMg_2O_4$	834	547	444	348	[74]

fluctuations), we follow the method proposed by Kumar-Fennie-Rabe for magnetic spinels [69]. In this method, we take the statistical average of the interatomic force constants calculated for all the possible spin configurations such that each Co-Co bond has an equal fraction of parallel and antiparallel spins. This method assumes that the timescale of phonons is much longer compared to the spin fluctuations, and spins in the paramagnetic phase are not correlated, which are reasonable approximations at the high-temperature limit. In the case of GCO, we have 4 magnetic Co atoms yielding a total of 2^4 (=16) collinear spin configurations, which can be reduced to 8 spin configurations using the time-reversal symmetry. A further consideration of the cubic crystal symmetry reduces the total number of nonequivalent spin configurations to three, which are $++++$, $++--$, and $+---$, each with a statistical weight of $\frac{1}{8}$, $\frac{3}{8}$, and $\frac{1}{2}$, respectively. Here, $+/-$ denotes the up/down spin moment at each Co site. Thus, the computed phonon frequencies for the IR-active and Raman-active modes are given in Tables I and II.

Owing to the fact that the PBEsol functional describes the lattice parameters and bond lengths in GCO better than the PBE functional, we find that the PBEsol predicted phonon frequencies are in better agreement with the experimental data compared to the PBE predictions.

1. IR-active modes

The frequencies of the four allowed IR-active modes in GCO along with those for some other normal spinels are listed in Table I. The Fourier-transform infrared (FTIR) spectrum of GCO recorded at 300 K in the transmission mode, shown in Fig. 5, displays the observation of the $T_{1u}(1)$, $T_{1u}(2)$, and $T_{1u}(3)$ modes at frequencies 680, 413, and 325 cm^{-1}, respectively, which are in decent agreement with our DFT+U

calculated frequencies. Since the experimental limitations did not allow us to measure modes below 300 cm^{-1}, the $T_{1u}(4)$ mode predicted to occur at 189 cm^{-1} (see Table I) could not be observed. However, the predicted frequency of the $T_{1u}(4)$ mode is in good agreement with the experimental data (186 cm^{-1}) reported by Preudhomme and Tarte [48]. Overall, there is a good agreement between the observed and predicted values for the IR-active modes at room temperature.

In addition to the above-listed IR-active modes, Fig. 5 shows the observation of two satellite modes at 608 and 459 cm^{-1}, marked as v_1 and v_2, respectively. Although crystal symmetry allows the observation of only four T_{1u} modes, these additional satellite modes are likely occurring from the splitting of the T_{1u} modes due to the induced local electric fields [68]. The presence of any impurity or crystallite domains in a powder sample breaks the local crystal symmetry distorting the local potential, which in turn relaxes the selection rules governing the observation of the allowed IR-active modes, and it may lead to the appearance of the satellite modes in the IR spectrum. Such satellite modes have been previously observed in lithium-cobalt oxides [70,71].

Our DFT+U calculations predict moderate spin-phonon coupling in the IR-active T_{1u} modes of GCO. We notice that each triply degenerate T_{1u} mode of the O_h point group splits into two modes, i.e., one doublet and one singlet, when the magnetic symmetry is changed from FM to AFM, which is consistent with the work of Wysocki and Birol [72]. The magnitude of the frequency splitting between the doublet and singlet modes ($\Delta\omega_{ds}$) provides a good qualitative estimate of the strength of the spin-phonon coupling in magnetic spinels [68,69,72,73]. In the case of GCO, the PBEsol+U (PBE+U) calculated $\Delta\omega_{ds}$ is 1 (1), 4 (2), 6 (10), and 2 (2) cm^{-1} for the $T_{1u}(1)$, $T_{1u}(2)$, $T_{1u}(3)$, and $T_{1u}(4)$ modes,

TABLE II. List of Raman-active phonon modes and their frequencies (in cm^{-1}) at room temperature for several cubic spinels

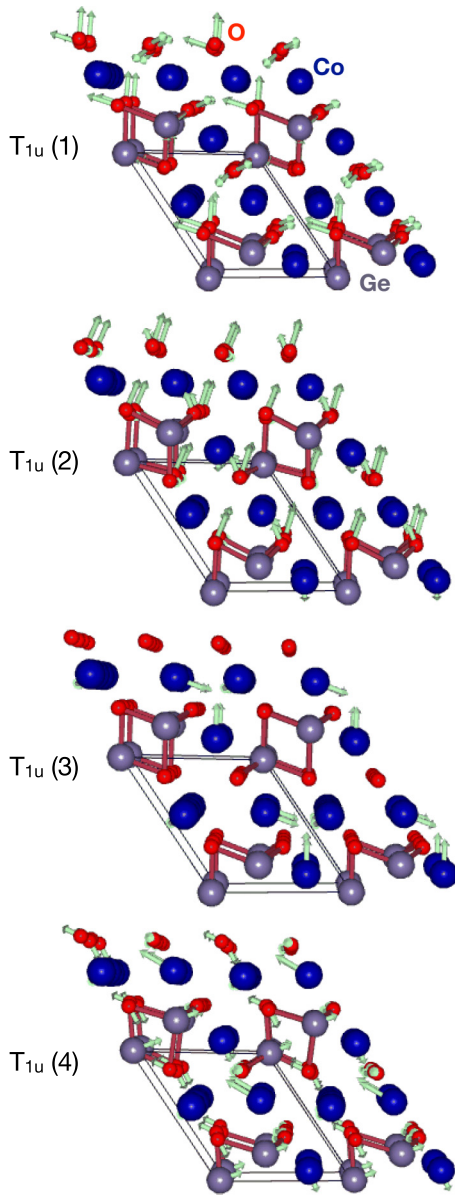|	A_{1g}	$T_{2g}(1)$	$T_{2g}(2)$	E_g	$T_{2g}(3)$	Reference
$GeCo_2O_4$	760	647	550	308		This work (Experiment)
$GeCo_2O_4$	# 720	649	475	323	204	This work (Calculation)
	* (695)	(610)	(461)	(311)	(203)	# PBEsol+U; * (PBE+U)
$GeCo_2O_4$	757	643		302		[47]
$SiCo_2O_4$	833	788	521	373	270	[74]
$GeMg_2O_4$	777	669	520	341	213	[75]
$SiMg_2O_4$	834	798	599	373	300	[74]
$MgTi_2O_4$	628	493	335	448		[76]

FIG. 3. Atomic vibration patterns for all four IR-active phonon modes: (i) $T_{1u}(1)$, (ii) $T_{1u}(2)$, (iii) $T_{1u}(3)$, and (iv) $T_{1u}(4)$. The color coding of atoms is the same as in Fig. 1(a). These modes are listed here in the order of decreasing frequency (see Table I).

FIG. 4. Atomic vibration patterns for all five Raman-active phonon modes: A_{1g}, $T_{2g}(1)$, $T_{2g}(2)$, E_g, and $T_{2g}(3)$. These modes are listed here in the order of decreasing frequency (see Table II).

respectively. These values are consistent with the previously reported data on other magnetic spinels [68,69,72,73]. The maximum frequency splitting is predicted for the $T_{1u}(3)$ mode, which is evident since the $T_{1u}(3)$ mode involves the vibration of the magnetic Co sites, as shown in Fig. 3. An experimental validation of the aforementioned frequency-splitting values requires low-temperature IR measurements, which, unfortunately, could not be carried out because of the limitations of our experimental facilities.

The high-frequency IR-active modes $T_{1u}(1)$ and $T_{1u}(2)$, as shown in Fig. 3, involve the symmetric and asymmetric bending of oxygen ions present at the tetrahedral and octahedral sites, whereas the low-frequency IR-active modes, $T_{1u}(3)$ and $T_{1u}(4)$, are associated with the vibrations of the
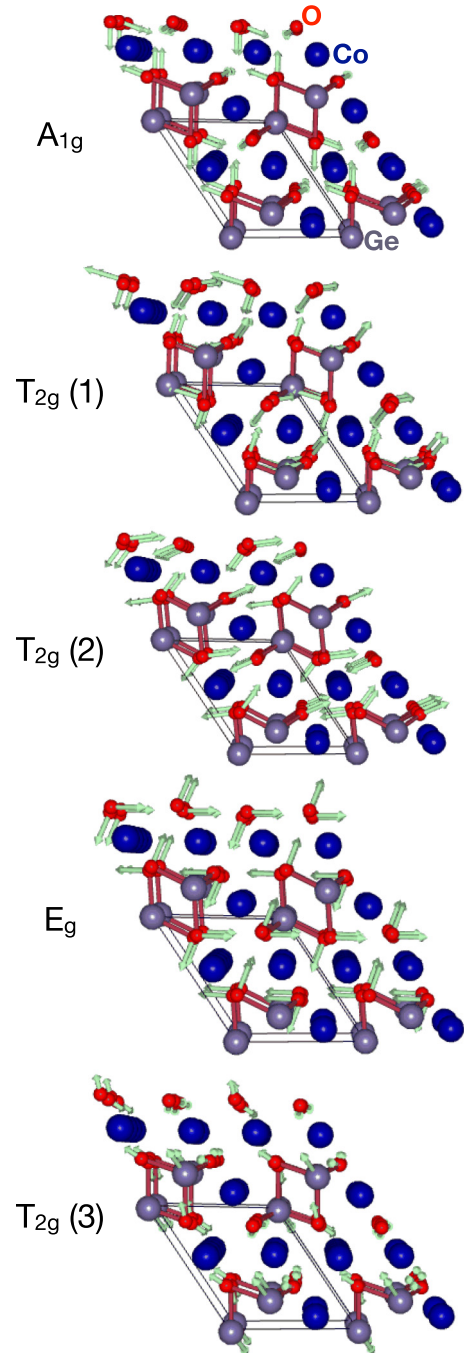
relatively heavier Ge and Co ions situated at the tetrahedral and octahedral sites, respectively. Generally, the frequency of a mode varies as $\sqrt{k/m}$, where k is the stiffness constant of the bond and m is the effective mass of the associated ions. From the magnitudes of the four IR-active modes for various spinels listed in Table I, one can argue that the $T_{1u}(1)$ and $T_{1u}(2)$ modes are due to the vibrations of the tetrahedral group (GeO$_4$ or SiO$_4$), whereas $T_{1u}(3)$ and $T_{1u}(4)$ also involve the vibrations of the octahedral group (MgO$_6$ and CoO$_6$). Our reasoning is as follows: When Co in GeCo$_2$O$_4$ is replaced by lighter Mg in GeMg$_2$O$_4$, there is an increase of about 50% in
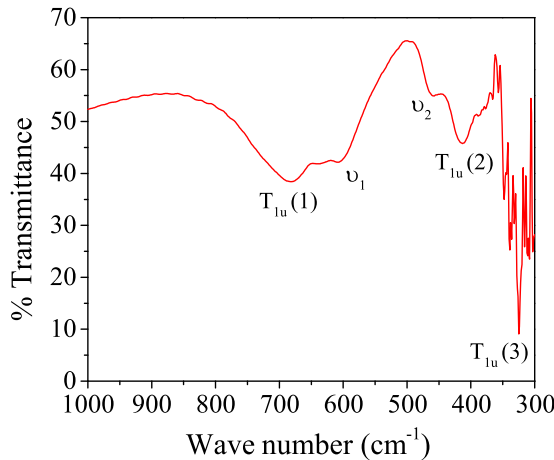
FIG. 5. Fourier-transform infrared spectrum of GCO polycrystalline sample recorded at room temperature. The DFT+U simulated IR spectrum is given in the SM [54].

FIG. 6. Raman spectra of GCO recorded at temperatures $T = 5$, 10, 12, 14, 18, 20, 21, 22, 24, 26, 30, 40, 60, 80, 100, and 300 K.

the frequencies of the $T_{1u}(3)$ and $T_{1u}(4)$ modes, whereas the increase in the frequencies of the $T_{1u}(1)$ and $T_{1u}(2)$ modes is only a few percent. When lighter Si in SiCo$_2$O$_4$ replaces heavier Ge in GeCo$_2$O$_4$, the frequencies of the $T_{1u}(1)$ and $T_{1u}(2)$ modes in SiCo$_2$O$_4$ go up by about 25%, whereas the change in the $T_{1u}(3)$ and $T_{1u}(4)$ mode frequencies is only about 5%. Therefore, the $T_{1u}(1)$ and $T_{1u}(2)$ modes primarily represent the vibrations of the tetrahedral group, while the $T_{1u}(3)$ and $T_{1u}(4)$ modes represent the vibrations of the octahedral group. This qualitative description is consistent with the schematic phonon eigenvectors plot shown in Fig. 3.

2. Raman-active modes

The frequencies of the Raman-active modes in GCO (at 300 K) are listed in Table II along with their calculated values. As done in Table I for the IR modes, we have also listed the frequencies of the Raman-active modes in Table II reported for several other isostructural spinels, e.g., SiCo$_2$O$_4$, GeMg$_2$O$_4$, MgTi$_2$O$_4$, and SiMg$_2$O$_4$. Our observed values of the frequencies of A_{1g}, $T_{2g}(1)$, and E_g modes in GCO are nearly identical to those reported by Koningstein *et al.* [47]. Here we additionally report the frequency of the $T_{2g}(2)$ mode in GCO. Our DFT+U calculated phonon frequencies of Raman-active modes are in good agreement with the experimental observations. The $T_{2g}(3)$ mode could not be detected in our experiments since this mode is predicted to occur below the lowest frequency of our Raman measurements. However, the predicted frequency of the $T_{2g}(3)$ mode is consistent with that of reported values for other isostructural spinel oxides (see Table II).

Our calculations reveal that the strength of the spin-phonon coupling is the largest for the $T_{2g}(3)$ mode since this mode is associated with the vibration of the heavy cations. The values of the frequency splitting $\Delta\omega_{ds}$ for the triply degenerate $T_{2g}(1)$, $T_{2g}(2)$, and $T_{2g}(3)$ modes are 3 (1), 2 (2), and 5 (3) cm^{-1}, respectively, as obtained using the PBEsol+U (PBE+U) method. We note that these values are in the same range of the observed frequency shifts of the associated Raman peaks at T_N, as discussed below.
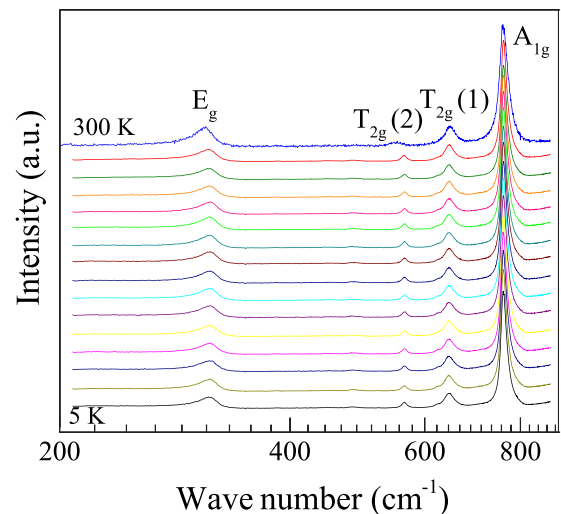
To better understand the Raman modes in GCO, a systematic comparison of their frequencies with those reported in SiCo$_2$O$_4$, GeMg$_2$O$_4$, SiMg$_2$O$_4$, and MgTi$_2$O$_4$ are listed in Table II. Comparing SiCo$_2$O$_4$ with GeCo$_2$O$_4$ for which the lighter Si atom replaces the heavier Ge atom at the tetrahedral site, the frequencies of the A_{1g}, E_g, and $T_{2g}(1)$ modes in SiCo$_2$O$_4$ are increased by about 10–20%. This suggests that these modes likely involve some motion of the tetrahedral cation in addition to the O atoms. This is further confirmed by comparing the mode frequencies of GeMg$_2$O$_4$ with those in SiMg$_2$O$_4$, where the frequencies of the A_{1g}, E_g, and $T_{2g}(1)$ modes in SiMg$_2$O$_4$ are higher by about 10–20%. For the $T_{2g}(2)$ mode, the observed differences in the frequencies for GCO vis-à-vis SiCo$_2$O$_4$, GeMg$_2$O$_4$, and SiMg$_2$O$_4$ do not show a systematic pattern. To further understand the role of the Co-O octahedra on the Raman modes, mode frequencies in GeMg$_2$O$_4$ and GeCo$_2$O$_4$ are compared in which the lighter Mg replaces the heavier Co. In this case, the frequencies of the A_{1g} and $T_{2g}(1)$ modes are increased only by about 2%. However, the frequency of the E_g mode in GeMg$_2$O$_4$ is enhanced by about 11%. This suggests that the E_g mode also involves some vibrations of the cations on the octahedral site. In summary, for GCO, the A_{1g} and $T_{2g}(1)$ modes involve some vibrations of Ge at the tetrahedral site in addition to the vibrations of the O atoms, whereas for the E_g modes, the vibrations of GeO$_4$ and CoO$_6$ are also involved.

In Fig. 7, we compare the DFT+U predicted phonon frequencies calculated for the paramagnetic phase using the statistical averaging method, as mentioned above, with the experimental data recorded at 300 K from the IR and Raman measurements. The experimental frequency of the $T_{1u}(4)$ mode was obtained from Ref. [48]. We observe a good agreement between theory and experiment. In particular, the PBEsol+U predicted frequencies are in better agreement with the experimental data compared to the PBE+U predictions.

3. Temperature dependence of the Raman-active modes

A brief summary of the temperature dependence of the structural properties of GCO is first presented in order to place
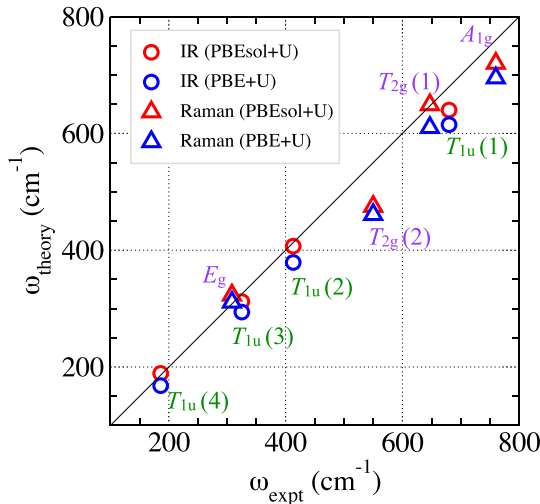
FIG. 7. Comparison of the DFT+U predicted phonon frequencies (ω_{theory}) for the simulated paramagnetic phase with the experimentally measured frequencies at 300 K (ω_{expt}) for the IR- and Raman-active modes. The data plotted in this figure were obtained from Tables I and II.

the data on the Raman-active modes in proper context. Using x-ray synchrotron data on a polycrystal GCO, Barton *et al.* [26] determined changes in the lattice parameters and Co-O and Ge-O bond lengths as a function of temperature, including the regions around $T_N = 21$ K and $T_S = 16$ K. For $T < T_S$, the crystal symmetry changes from cubic to tetragonal with $c/a > 1$ with the degree of tetragonality increasing with decreasing T. An elongation of the CoO$_6$ octahedron is observed below the T_S as the Co-O bond length equal to 2.09 Å above T_N increases to 2.13 Å along the c axis, but decreases to 2.07 Å normal to the c axis for $T < T_S$. However, there is no change in the Ge-O bond length in the GeO$_4$ tetrahedron as the symmetry changes from the cubic to tetragonal phase below the T_S. Considering these results, changes around T_S should be expected in the Raman- and the IR-active modes which involve vibrations of the atoms in the CoO$_6$ octahedron.

The structural transition at low temperature is expected due to the possible Jahn-Teller distortions and spin-orbit coupling effects in the $3d^7$ state of Co^{2+}, in which the spin degeneracy is lifted due to the stabilization of the t_{2g} orbitals. Following our earlier discussion of the comparison of the Raman-active modes for different spinels listed in Table II, significant changes around T_S should be expected for the E_g mode. Another relevant and important result from the paper by Barton *et al.* [26] is the presence of the magneto-dielectric coupling, which is evident from the fitting of the temperature-dependent dielectric constant data of GCO with the Barrett equation for $T > T_N$ (similar to previous reports on MnO and MnF$_2$ [77–79]) yielding 339 cm^{-1} as the frequency of the coupling mode. This frequency is close to that of the E_g mode determined in this work.

Keeping the above comments in mind, the Raman spectra of GCO recorded at various temperatures between 5 and 300 K are shown in Fig. 6, with each line identified with one of the five Raman-active modes. For each line, except the $T_{2g}(3)$ mode whose intensity is too weak for accurate
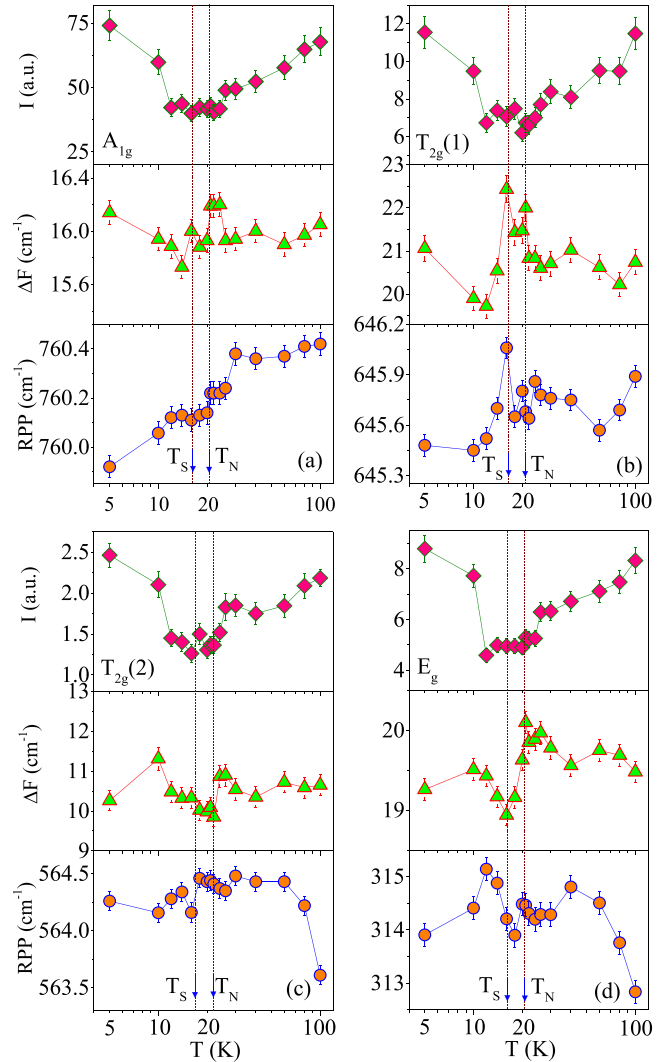

FIG. 8. The temperature dependence of Raman intensity (I × 10^4), full width at half maximum (ΔF), and Raman-peak position (RPP) for the A_{1g}, $T_{2g}(1)$, $T_{2g}(2)$, and E_g Raman-active modes. The lines connecting the data points are visual guides. The T_N and T_S mark the transition temperatures corresponding to the antiferromagnetic and the cubic-to-tetragonal structural phase transitions, respectively.

measurements, we measured its position, full width at half maximum (FWHM), and line intensity (area under the peak), and plotted these quantities as a function of temperature in Fig. 8. The positions of $T_N = 21$ K and $T_S = 16$ K are also marked by vertical dashed lines in these plots. Qualitative interpretations of these results are presented below.

A detailed examination of the plots shown in Fig. 8 reveals some interesting features. First, for all four observed Raman modes, viz., A_{1g}, E_g, $T_{2g}(1)$, and $T_{2g}(2)$, the intensity of the Raman lines increases with decreasing temperature below T_S, which is somewhat similar to the variation of the order parameter. According to the Suzuki and Kamimura theory [80] for the spin-dependent Raman scattering, the magnetic order significantly influences the phonon Raman efficiency through the dependence of the optical dipole transitions on the relative orientation of the adjacent spins. Generally, the
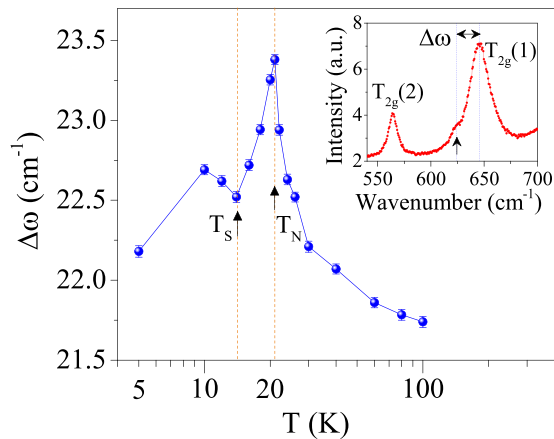
FIG. 9. The temperature dependence of the line separation $\Delta\omega$ of the low-frequency shoulder from the position of the $T_{2g}(1)$ peak. Inset: the shoulder appearing on the low-frequency side of the $T_{2g}(1)$ peak.

temperature dependence of the integrated Raman intensity is proportional to the nearest-neighbor spin correlation function [81]. Also, the emergence of an AFM order below the T_N enhances the Raman intensity due to the Brillouin-zone folding since the magnetic unit cell would be doubled in size compared to the structural unit cell [80,81]. As a result, the Raman intensity always enhances below the magnetic transition in both FM and AFM systems.

The second noticeable effect is the dramatic changes observed in the FWHM for the $T_{2g}(1)$, $T_{2g}(2)$, and E_g modes between T_N and T_S along with weaker anomalies in the line positions of these modes. As argued earlier based on the comparison with data on other spinels, significant changes due to the structural transition at T_S were expected in the line parameters of the E_g mode. The results presented in Fig. 8 show that the effects of magnetic ordering at T_N and structural transition at T_S for the $T_{2g}(1)$, $T_{2g}(2)$, and E_g modes are significant.

The Raman linewidth is supposed to decrease with decreasing temperature since the phonon scattering usually gets suppressed at low temperatures. As can be noticed from Fig. 8, the FWHM (ΔF) is indeed decreasing below T_N until T_S, which clearly indicates that the structural transition is independent of the magnetic transition. Also, for the only case of $T < T_S$, there is (roughly) an overall increase in the FWHM of all four Raman-active modes. This could be associated to the cubic-to-tetragonal structural distortion occurring at T_S since this distortion could lift the degeneracy of the degenerate Raman-active modes, with the exception of the nondegenerate A_g mode. It is possible that the distortion-split modes are not showing up distinctly in our Raman measurements due to their smaller magnitude of the frequency shift; however, they may form a convoluted peak with a larger FWHM. Another possible explanation could be related to the local structural disorder driven by the randomly distributed Ge atoms, which may cause an increase in the linewidth at $T < T_S$.

Another noteworthy feature evident from the Raman spectra at low temperatures is the separation of a shoulder, marked by an arrow in the inset of Fig. 9, on the low-frequency side of the $T_{2g}(1)$ line. The origin of this shoulder is not yet

well understood. However, we think it could be attributed to the magnon-induced excitations [82]. In Fig. 9, we plot the temperature dependence of the frequency shift of this shoulder $\Delta\omega$ from the $T_{2g}(1)$ line. We note that $\Delta\omega$ increases with lowering temperature and attains a maximum value at T_N. With a further decrease in temperature ($T_S < T < T_N$), $\Delta\omega$ starts decreasing, and it shows an upturn at T_S.

Such a temperature dependence of $\Delta\omega$ implies the presence of two distinct phase transitions, i.e., one magnetic and another structural, in GCO, thus validating the claim of Barton *et al.* [26] that the structural phase transition in GCO does not occur exactly at T_N, rather it follows the magnetic phase transitions at 21 K and occurs at 16 K. Our DFT+U calculations further support this argument as we do not notice any phonon instability when the magnetic order is changed from FM to AFM. This suggests that no structural phase transition should occur exactly at T_N. However, below T_N, the system could undergo a structural phase transition due to the relaxation of stress and forces on atoms within the AFM phase [69].

IV. CONCLUSIONS

Results from our combined experimental and computational investigations of the IR- and Raman-active modes of the normal spinel GeCo$_2$O$_4$ with the effective spin $S = 1/2$ ground state have been presented here with the following major conclusions: (i) The measured frequencies of the IR- and Raman-active modes at room temperature are in good agreement with the results obtained from our DFT+U calculations. (ii) All the IR- and Raman-active modes exhibit moderate spin-phonon coupling in GeCo$_2$O$_4$. (iii) The temperature dependence of the Raman-active modes carried out between 5 and 100 K with special attention given to the region between T_N ($\sim$21 K) and T_S ($\sim$16 K) shows noticeable anomalies in the line parameters of the Raman-active modes. (iv) The temperature-dependent frequency shift of a shoulder appearing near the peak of the Raman-active mode $T_{2g}(1)$ validates that the structural phase transition in GeCo$_2$O$_4$ is distinct from the magnetic phase transition occurring at T_N. Investigation of the temperature dependence of the IR modes covering the region below T_N is recommended since it is likely to provide significant information on the transitions at T_N and T_S.

Our DFT+U calculations reveal that exchange interactions up to at least the third-nearest neighbors are required to correctly describe the low-temperature antiferromagnetic ordering in GeCo$_2$O$_4$. We find that the nearest-neighbor magnetic-exchange interaction has a ferromagnetic nature and is a superexchange interaction mediated via an intermediate oxygen ion having a Co-O-Co bond angle of $\theta = 90°$. Instead, the second- and third-nearest-neighbor exchange interactions are antiferromagnetic in nature, and they involve more than one ion along the exchange-interaction path corresponding to the super-super-exchange interaction. These interactions play a vital role in stabilizing the ($\mathbf{q} = \frac{1}{2}, \frac{1}{2}, \frac{1}{2}$) antiferromagnetic order in GeCo$_2$O$_4$ at low temperatures.

The presence of the spin $S = 1/2$ ground state in GeCo$_2$O$_4$ due to spin-orbit coupling and local Jahn-Teller distortion effects, discussed in detail in Ref. [15], gets additional support

from the recently reported results of an Ising linear chain system $CoNb_2O_6$ having a similar $S = 1/2$ ground state of Co^{2+} ions [83]. Lastly, we note that inclusion of the spin-orbit coupling and local Jahn-Teller distortion effects in DFT+U calculations may slightly change the quantitative values reported in this work without affecting the overall physics of the studied system.

[1] A. H. Morrish, *Physical Principles of Magnetism* (IEEE Press, New York, 2001), p. 503.

[2] K. M. Rabe, Annu. Rev. Condens. Matter Phys. **1**, 211 (2010).

[3] N. T. Thanh, *Magnetic Nanoparticles: From Fabrication to Clinical Applications* (CRC, Boca Raton, FL, 2012).

[4] J. Chakhalian, J. W. Freeland, A. J. Millis, C. Panagopoulos, and J. M. Rondinelli, Rev. Mod. Phys. **86**, 1189 (2014).

[5] M. S. Seehra, in *Magnetic Spinels: Synthesis, Properties and Applications*, edited by M. S. Seehra (Intech Publishers, London, UK, 2017).

[6] S. Thota and S. Singh, in *Magnetic Spinels: Synthesis, Properties and Applications*, edited by M. S. Seehra (Intech Publishers, London, UK, 2017), Chap. 4.

[7] S. Singh, P. Pramanik, S. Sangaraju, A. Mallick, L. Giebeler, and S. Thota, J. Appl. Phys. **121**, 194303 (2017).

[8] P. Pramanik, S. Thota, S. Singh, D. C. Joshi, B. Weise, A. Waske, and M. S. Seehra, J. Phys.: Condens. Matter **29**, 425803 (2017).

[9] V. G. Harris, A. Geiler, Y. Chen, S. D. Yoon, M. Wu, A. Yang, Z. Chen, P. He, P. V. Parimi, X. Zuo *et al.*, J. Magn. Magn. Mater. **321**, 2035 (2009).

[10] P. W. Anderson, Phys. Rev. **102**, 1008 (1956).

[11] X. Liu, S. Singh, B. J. Kirby, Z. Zhong, Y. Cao, B. Pal, M. Kareev, S. Middey, J. W. Freeland, P. Shafer, E. Arenholz, D. Vanderbilt, and J. Chakhalian, Nano Lett. **19**, 8381 (2019).

[12] W. Schiessl, W. Potzel, H. Karzel, M. Steiner, G. M. Kalvius, A. Martin, M. K. Krause, I. Halevy, J. Gal, W. Schäfer, G. Will, M. Hillberg, and R. Wäppling, Phys. Rev. B **53**, 9143 (1996).

[13] M. S. Seehra, V. Singh, and S. Thota, J. Appl. Phys. **110**, 113907 (2011).

[14] S. Ghosh, S. Singh, D. C. Joshi, P. Pramanik, S. Ghosh, P. K. Mishra, and S. Thota, Phys. Rev. B **98**, 235119 (2018).

[15] P. Pramanik, S. Ghosh, P. Yanda, D. C. Joshi, S. Pittala, A. Sundaresan, P. K. Mishra, S. Thota, and M. S. Seehra, Phys. Rev. B **99**, 134422 (2019).

[16] X. Ge, S. Song, and H. Zhang, CrystEngComm **14**, 7306 (2012).

[17] S. Jin, G. Yang, H. Song, H. Cui, and C. Wang, ACS Appl. Mater. Interfaces **7**, 24932 (2015).

[18] Y. Subramanian, K. Kaliyappan, and K. S. Ramakrishnan, J. Colloid Interface Sci. **498**, 76 (2017).

[19] S. Yuvaraj, M.-S. Park, V. G. Kumar, Y. S. Lee, and D.-W. Kim, J. Electrochem. Sci. Technol. **8**, 323 (2017).

[20] S. Okubo, H. Ohta, T. Ijima, T. Yamasaki, W. Zhang, S. Hara, S. Ikeda, H. Oshima, M. Takahashi, K. Tomiyasu, and T. Watanabe, Z. Phys. Chem. **231**, 827 (2017).

[21] T. Yamasaki, S. Okubo, H. Ohta, T. Sakurai, S. Ikeda, H. Oshima, M. Takahashi, S. Hara, K. Tomiyasu, and T. Watanabe, J. Phys.: Conf. Ser. **400**, 032119 (2012).

[22] S. Diaz, S. de Brion, G. Chouteau, B. Canals, V. Simonet, and P. Strobel, Phys. Rev. B **74**, 092404 (2006).

[23] M. Matsuda, T. Hoshi, H. Aruga Katori, M. Kosaka, and H. Takagi, J. Phys. Soc. Jpn. **80**, 034708 (2011).

[24] Y. Horibe, M. Shingu, K. Kurushima, H. Ishibashi, N. Ikeda, K. Kato, Y. Motome, N. Furukawa, S. Mori, and T. Katsufuji, Phys. Rev. Lett. **96**, 086406 (2006).

[25] J. C. Lashley, R. Stevens, M. K. Crawford, J. Boerio-Goates, B. F. Woodfield, Y. Qiu, J. W. Lynn, P. A. Goddard, and R. A. Fisher, Phys. Rev. B **78**, 104406 (2008).

[26] P. T. Barton, M. C. Kemei, M. W. Gaultois, S. L. Moffitt, L. E. Darago, R. Seshadri, M. R. Suchomel, and B. C. Melot, Phys. Rev. B **90**, 064105 (2014).

[27] X. Fabrèges, E. Ressouche, F. Duc, S. de Brion, M. Amara, C. Detlefs, L. Paolasini, E. Suard, L.-P. Regnault, B. Canals, P. Strobel, and V. Simonet, Phys. Rev. B **95**, 014428 (2017).

[28] K. Tomiyasu, M. K. Crawford, D. T. Adroja, P. Manuel, A. Tominaga, S. Hara, H. Sato, T. Watanabe, S. I. Ikeda, J. W. Lynn, K. Iwasa, and K. Yamada, Phys. Rev. B **84**, 054405 (2011).

[29] X. Liu, S. Singh, V. Drouin-Touchette, T. Asaba, J. Brewer, Q. Zhang, Y. Cao, B. Pal, S. Middey, P. A. Kumar *et al.*, Nano Lett. **21**, 2010 (2021).

[30] J. Chakhalian, X. Liu, and G. A. Fiete, APL Mater. **8**, 050904 (2020).

[31] T. Hoshi, H. A. Katori, M. Kosaka, and H. Takagi, J. Magn. Magn. Mater. **310**, e448 (2007).

[32] T. Watanabe, S. Hara, and S.-I. Ikeda, Phys. Rev. B **78**, 094420 (2008).

[33] S. Ghosh, S. Singh, D. Das, S. Ghosh, P. K. Mishra, and S. Thota, J. Phys.: Condens. Matter **33**, 145504 (2021).

[34] S. Bordács, D. Varjas, I. Kézsmárki, G. Mihály, L. Baldassarre, A. Abouelsayed, C. A. Kuntscher, K. Ohgushi, and Y. Tokura, Phys. Rev. Lett. **103**, 077205 (2009).

[35] S. Thota, K. Singh, S. Nayak, C. Simon, J. Kumar, and W. Prellier, J. Appl. Phys. **116**, 103906 (2014).

[36] C. Kim, E. Jo, B. Kang, S. Kwon, S. Lee, J. H. Shim, T. Suzuki, and T. Katsufuji, Phys. Rev. B **86**, 224420 (2012).

[37] M. Kim, X. M. Chen, X. Wang, C. S. Nelson, R. Budakian, P. Abbamonte, and S. L. Cooper, Phys. Rev. B **84**, 174424 (2011).

[38] F. Guillou, S. Thota, W. Prellier, J. Kumar, and V. Hardy, Phys. Rev. B **83**, 094423 (2011).

[39] M. R. Suchomel, D. P. Shoemaker, L. Ribaud, M. C. Kemei, and R. Seshadri, Phys. Rev. B **86**, 054406 (2012).

[40] S. Thota, M. Reehuis, A. Maljuk, A. Hoser, J.-U. Hoffmann, B. Weise, A. Waske, M. Krautz, D. C. Joshi, S. Nayak, S. Ghosh, P. Suresh, K. Dasari, S. Wurmehl, O. Prokhnenko, and B. Büchner, Phys. Rev. B **96**, 144104 (2017).

[41] S. Nayak, S. Thota, D. C. Joshi, M. Krautz, A. Waske, A. Behler, J. Eckert, T. Sarkar, M. S. Andersson, R. Mathieu, V. Narang, and M. S. Seehra, Phys. Rev. B **92**, 214434 (2015).

[42] S. Nayak, K. Dasari, D. Joshi, P. Pramanik, R. Palai, A. Waske, R. Chauhan, N. Tiwari, T. Sarkar, and S. Thota, J. Appl. Phys. **120**, 163905 (2016).

[43] S. Nayak, D. Joshi, M. Krautz, A. Waske, J. Eckert, and S. Thota, J. Appl. Phys. **119**, 043901 (2016).

[44] P. Pramanik, D. C. Joshi, M. Reehuis, A. Hoser, J. Hoffmann, R. Manna, T. Sarkar, and S. Thota, J. Phys.: Condens. Matter **32**, 245801 (2020).

[45] S. Thota, V. Narang, S. Nayak, S. Sambasivam, B. Choi, T. Sarkar, M. S. Andersson, R. Mathieu, and M. S. Seehra, J. Phys.: Condens. Matter **27**, 166001 (2015).

[46] S. Thota and M. S. Seehra, J. Appl. Phys. **113**, 203905 (2013).

[47] J. Koningstein, P. Grunberg, J. Hoff, and J. Preudhomme, J. Chem. Phys. **56**, 354 (1972).

[48] J. Preudhomme and P. Tarte, Spectrochim. Acta Part A: Molec. Spectrosc. **28**, 69 (1972).

[49] G. Kresse and J. Furthmüller, Phys. Rev. B **54**, 11169 (1996).

[50] G. Kresse and J. Furthmüller, Comput. Mater. Sci. **6**, 15 (1996).

[51] G. Kresse and D. Joubert, Phys. Rev. B **59**, 1758 (1999).

[52] H. J. Monkhorst and J. D. Pack, Phys. Rev. B **13**, 5188 (1976).

[53] U. Herath, P. Tavadze, X. He, E. Bousquet, S. Singh, F. Muñoz, and A. H. Romero, Comput. Phys. Commun. **251**, 107080 (2020).

[54] See Supplemental Material at http://link.aps.org/supplemental/10.1103/PhysRevB.104.014433 for the simulated IR spectrum, and total energies of different spin configurations along with the calculated densities of states.

[55] A. Togo and I. Tanaka, Scr. Mater. **108**, 1 (2015).

[56] J. P. Perdew, K. Burke, and M. Ernzerhof, Phys. Rev. Lett. **77**, 3865 (1996).

[57] J. P. Perdew, A. Ruzsinszky, G. I. Csonka, O. A. Vydrov, G. E. Scuseria, L. A. Constantin, X. Zhou, and K. Burke, Phys. Rev. Lett. **100**, 136406 (2008).

[58] A. I. Liechtenstein, V. I. Anisimov, and J. Zaanen, Phys. Rev. B **52**, R5467(R) (1995).

[59] B. Meredig, A. Thompson, H. A. Hansen, C. Wolverton, and A. van de Walle, Phys. Rev. B **82**, 195128 (2010).

[60] J. P. Allen and G. W. Watson, Phys. Chem. Chem. Phys. **16**, 21016 (2014).

[61] P. W. Anderson, Phys. Rev. **79**, 350 (1950).

[62] J. B. Goodenough, Phys. Rev. **100**, 564 (1955).

[63] J. B. Goodenough, J. Phys. Chem. Solids **6**, 287 (1958).

[64] J. Kanamori, J. Phys. Chem. Solids **10**, 87 (1959).

[65] J. Kanamori, J. Appl. Phys. **31**, S14 (1960).

[66] R. D. Waldron, Phys. Rev. **99**, 1727 (1955).

[67] W. White and B. DeAngelis, Spectrochim. Acta A **23**, 985 (1967).

[68] K. T. Chan, J. D. Sau, P. Zhang, and M. L. Cohen, Phys. Rev. B **75**, 054304 (2007).

[69] A. Kumar, C. J. Fennie, and K. M. Rabe, Phys. Rev. B **86**, 184429 (2012).

[70] C. M. Burba, K. Shaju, P. G. Bruce, and R. Frech, Vibration. Spectrosc. **51**, 248 (2009).

[71] P. Ahamed and M. A. Yousuf, Mater. Res. Express **7**, 065506 (2020).

[72] A. L. Wysocki and T. Birol, Phys. Rev. B **93**, 134425 (2016).

[73] C. J. Fennie and K. M. Rabe, Phys. Rev. Lett. **96**, 205505 (2006).

[74] A. Kushwaha, C.-G. Ma, M. Brik, and S. Akbudak, J. Phys. Chem. Solids **117**, 167 (2018).

[75] N. L. Ross and A. Navrotsky, Phys. Chem. Miner. **14**, 473 (1987).

[76] Z. V. Popović, G. De Marzi, M. J. Konstantinović, A. Cantarero, Z. Dohčević-Mitrović, M. Isobe, and Y. Ueda, Phys. Rev. B **68**, 224302 (2003).

[77] M. S. Seehra and R. E. Helmick, Phys. Rev. B **24**, 5098 (1981).

[78] M. S. Seehra and R. Helmick, J. Appl. Phys. **55**, 2330 (1984).

[79] M. S. Seehra, R. Helmick, and G. Srinivasan, J. Phys. C: Solid State Phys. **19**, 1627 (1986).

[80] N. Suzuki and H. Kamimura, J. Phys. Soc. Jpn. **35**, 985 (1973).

[81] M. Balkanski, M. Jouanne, and M. Scagliotti, Pure Appl. Chem. **59**, 1247 (1987).

[82] A. Zhang, C. Liu, C. Yi, G. Zhao, T.-l. Xia, J. Ji, Y. Shi, R. Yu, X. Wang, C. Chen, and Q. Zhang, Nat. Commun. **7**, 13833 (2016).

[83] S. Thota, S. Ghosh, Maruthi R, D. C. Joshi, R. Medwal, R. S. Rawat, and M. S. Seehra, Phys. Rev. B **103**, 064415 (2021).